Materials and Design 165 (2019) 107598

Contents lists available at ScienceDirect

Materials and Design

journal homepage: www.elsevier.com/locate/matdes

# Microstructure and mechanical properties of Hastelloy X produced by HP-SLM (high power selective laser melting)

Maria L. Montero-Sistiaga [a,b,*], Saeid Pourbabak [a,c], Jan Van Humbeeck [a], Dominique Schryvers [c], Kim Vanmeensel [a]

[a] KU Leuven, Department of Materials Engineering, Kasteelpark Arenberg 44, Heverlee B-3001, Belgium
[b] ENGIE Laborelec, Rodestraat 125, Linkebeek B-1630, Belgium
[c] EMAT, University of Antwerp, Groenenborgerlaan 171, Antwerp B–2020, Belgium

## HIGHLIGHTS

- Using high power selective laser melting increases the productivity from 6 $mm^3/s$ to 16 $mm^3/s$ build rate.
- High power laser leads to coarser microstructure and induces a stronger morphological and crystallographic texture.
- Hot isostatic post processing leads to pore and crack closure as well as improved mechanical performance.
- Hot isostatic pressing maintains the sub-grain microstructure with slight coarsening and lower dislocation density.

## GRAPHICAL ABSTRACT

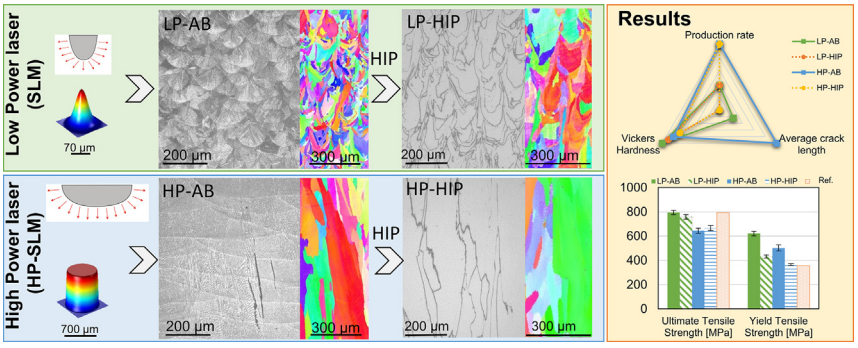


## ARTICLE INFO

*Article history:*
Received 25 October 2018
Received in revised form 19 December 2018
Accepted 8 January 2019
Available online 9 January 2019

*Keywords:*
High power selective laser melting
Additive manufacturing
Solidification microstructure
Hastelloy X
Hot isostatic pressing

## ABSTRACT

In order to increase the production rate during selective laser melting (SLM), a high power laser with a large beam diameter is used to build fully dense Hastelloy X parts. Compared to SLM with a low power and small diameter beam, the productivity was increased from 6 $mm^3/s$ to 16 $mm^3/s$, i.e. 2.6 times faster. Besides the productivity benefit, the influence of the use of a high power laser on the rapid solidification microstructure and concomitant material properties is highlighted. The current paper compares the microstructure and tensile properties of Hastelloy X built with low and high power lasers. The use of a high power laser results in wider and shallower melt pools inducing an enhanced morphological and crystallographic texture along the building direction (BD). In addition, the increased heat input results in coarser sub-grains or high density dislocation walls for samples processed with a high power laser. Additionally, the influence of hot isostatic pressing (HIP) as a post-processing technique was evaluated. After HIP, the tensile fracture strain increased as compared to the strain in the as-built state and helped in obtaining competitive mechanical properties as compared to conventionally processed Hastelloy X parts.

© 2019 Elsevier Ltd. This is an open access article under the CC BY-NC-ND license (http://creativecommons.org/licenses/by-nc-nd/4.0/).

## 1. Introduction

Selective laser melting (SLM) is a powder bed based additive manufacturing (AM) technique. The metallic powder is spread over a platform and a highly focused laser beam selectively melts a predefined

* Corresponding author at: KU Leuven, Department of Materials Engineering, Kasteelpark Arenberg 44, Heverlee B-3001, Belgium.
*E-mail address:* maria.montero@kuleuven.be (M.L. Montero-Sistiaga).

https://doi.org/10.1016/j.matdes.2019.107598
0264-1275/© 2019 Elsevier Ltd. This is an open access article under the CC BY-NC-ND license (http://creativecommons.org/licenses/by-nc-nd/4.0/).

2D layer [1]. Then, the platform is lowered according to the layer thickness. This process is repeated layer by layer until the completion of the final 3D solid part. The main advantages of this process are: the near-net-shaping capability, the geometrical complexity of the producible parts and the fast time-to-market compared to parts made by a combination of more conventional manufacturing and machining processes [1,2].

Within the last decade significant progress, related to different aspects of the SLM process, ranging from extending the material pallet towards machine design and development, has been realized. Initially, stainless steels and titanium based alloys covered the majority of the SLM research work [3,4]. Nowadays, however, the material's palette has been expanded to many aluminium alloys, titanium alloys, nickel based superalloys etc. [5–11]. Regarding the machine characteristics, thanks to the parallel development of fibre lasers, much higher laser powers can be used to accelerate the productivity [12,13] yielding a new generation of high power SLM (HP-SLM) machines. In addition, some machines are also equipped with a base plate preheating unit in order to reduce thermal stresses [14–16]. However, despite the aforementioned evolution, resulting in both material and machine improvements, there are still challenges to solve, such as the cracking tendency of certain materials [7,17].

Hastelloy X is a solid solution strengthened Nickel base superalloy which is characterized by its high oxidation resistance and high strength at elevated temperatures. It has been widely used in gas turbine engines and in the chemical processing industry.

Up to now, only a limited amount of investigations have been conducted on SLM of Hastelloy X. A major problem is the cracking found during SLM [17–19]. Similarly to welding, the generation of cracks is influenced by the existence of high solidification rates. Laser welding of Hastelloy has been studied using a Nd-YAG laser [20] and hot cracking was observed [21]. Due to the fact that both SLM and laser welding involve a local melting and rapid solidification process, welding and SLM microstructures are very similar. In both cases, after melting and rapid cooling of Hastelloy X, columnar dendritic microstructures are obtained. The mechanical properties of as-built (AB) parts processed by SLM showed that the yield strength and hardness was much higher than conventionally produced Hastelloy X [18,22]. Different authors, however, have mentioned the susceptibility to cracking of Hastelloy X during the SLM process [17,19,21].

In order to reduce the generation and propagation of cracks, most investigations have focused on modifying the alloy composition, specifically looking at the influence of each alloying element. Tomus et al. [17] found that a reduction of the Mn and Si content within the starting material reduces the cracking significantly due to a lower micro segregation of those elements at grain boundaries where cracks tend to initiate. However, Harrison et al. [19] doubted this theory as they found no increase of Si or Mn at the crack edge after elemental analysis using Energy Dispersive X-ray Spectroscopy (EDS). In contrast, Harrison et al. [19] suggested that the material's resistance to cracking could be related to the material's thermal shock resistance and hence to the ultimate tensile strength. Therefore, they proposed a modified Hastelloy composition with increased solid solution strengthening elements (e.g. Co, W and Mo) and reduced Mn and C. In this way, a 57% reduction in crack density was achieved.

Up to now, fundamental understanding of how new generation SLM machines, equipped with multiple lasers, interact with powder beds and influence the solidification behaviour, is still lacking. Furthermore, the interrelationship between the generated microstructures and the resulting material properties has not yet been investigated. In this paper, a commercial SLM machine (SLM280HL, SLM Solutions) equipped with both a high power laser with top-hat laser power distribution and a low power laser with Gaussian distribution is utilized. The differences in solidification microstructure, pore characteristics and crack occurrence in Hastelloy X produced with high power SLM (HP-SLM) and low power SLM are evaluated. In addition, the microstructural changes are linked to the mechanical property variations. In order to close the cracks that were present after SLM, hot isostatic pressing (HIP) is performed as a post-processing method. Afterwards, the microstructure evolution and its relation with the modified mechanical properties is evaluated.

## 2. Material and experiments

In the present work, a SLM280hl machine from SLM Solutions (Germany) was used to build the parts. This machine is equipped with two lasers; (1) a low power laser with a maximum output power of 400 W, a Gaussian power distribution and spot size ($1/e^2$ value) of 70 μm and (2) a high power laser with a maximum output power of 1 kW, a top-hat power distribution and 700 μm spot size. The sample labelling is depicted in Table 1. All samples were built on a 100 °C preheated baseplate. Different cubes (1 × 1 × 1 cm) were built using an energy density between 20 and 160 J/mm$^3$ for both lasers for parameter optimisation. The energy density ($E$) is calculated based on Eq. (1).

$$E = \frac{P}{v * h_s * t} \quad [\mathrm{J/mm^3}] \tag{1}$$

where $P$ refers to the laser power [W], $v$ to the scan speed [mm/s], $h_s$ to the hatch spacing [μm] and $t$ to the layer thickness [μm].

The material used in this work was Hastelloy X powder supplied by SLM solutions (Germany) with particle sizes ranging from 10 to 45 μm. The composition is shown in Table 2.

For microstructural investigation, the cubes were sectioned parallel to the building direction (BD), in XZ direction (see Fig. 1). The samples were ground and polished using a diamond suspension of 3 and 1 μm subsequently. In order to reveal the microstructure, the samples were electrochemically etched in 10% oxalic acid during 20 s at 7 V. A Leica DMILM HC microscope was used for optical microscopy (OM). A Nova NanoSEM 450 scanning electron microscope (SEM) equipped with an electron back-scattered diffraction (EBSD) detector was used for more detailed microstructural characterization. All EBSD scans were collected using a 1 μm step size. An average confidence index between 0.60 and 0.75 was obtained for all recorded spectra. OIM Analysis™ software was used to calculate inverse pole figures (IPF), texture index and grain sizes. Grain sizes were measured from 3 EBSD scans of 1.5 × 3 mm$^2$ in size. For crack length measurements, OM images from a 1 cm$^2$ polished cross section were analysed using Image-J free software [23] and the average was considered.

The samples that were used for transmission electron microscopy (TEM) investigation were sliced into 500 μm thick plates parallel to the BD and further ground to ~120 μm thickness. Discs of 3 mm diameter were punched from the obtained plates and electropolished with a mixture of 90% ethanol and 10% perchloric acid at −10 °C using a Struers Tenupol twin-jet electropolishing equipment. A FEI Osiris instrument running at 200 kV was used for TEM, High Angle Annular Dark Field Scanning TEM (HAADF-STEM), and Energy-Dispersive X-ray spectroscopy (EDX).

Rectangular shaped bars were built in the horizontal direction for both lasers and later machined to the tensile bar shape. The tests were performed in an Intron 4505 machine with a maximum of 250 kN load cell according to the ASTM E 8 M standard with a 1 mm/min strain rate. A Future Tech FV-700 machine was used to measure the Vickers micro hardness with 0.5 kg load. Half of the samples were subjected

**Table 1**
Sample labels for samples built using low and high power laser beams, differentiating between the sample in the as built and hot isostatic pressed conditions.

| | Low power | High power |
|---|---|---|
| As built | LP-AB | HP-AB |
| Hot isostatic pressed | LP-HIP | HP-HIP |

**Table 2**
Composition of Hastelloy X powder used in weight percentage measured by ICP-Combustion method.

| Ni | Cr | Fe | Mo | Co | W | S | P | Si | Mn | C | Al | O |
|---|---|---|---|---|---|---|---|---|---|---|---|---|
| 46.42 | 22.7 | 18.9 | 9 | 2.02 | 0.71 | <0.003 | <0.01 | 0.14 | 0.02 | 0.057 | <0.01 | 0.018 |

to a hot isostatic pressing post process at 1155 °C for 3 h at Bodycote NV, Sint-Niklaas (Belgium). For easy reference, the samples were labelled as shown in Table 1.

## 3. Results

### 3.1. Optimization of SLM parameters

Cubes with different scanning parameters were built using both the low and high power laser. The relative densities of the samples are depicted in Fig. 2 with respect to the energy density of the lasers. For both lasers, the optimal energy density range yielding the highest relative density for the material is between 40 and 80 J/mm$^3$, slightly extended to lower energy density values for the low power laser processed samples and to higher energy density values for the samples built using high power laser.

The type of porosity varies depending on the applied laser energy density. Fig. 2 shows that a too high energy density leads to the presence of key-hole pores while a too low energy density results in unmolten areas. Key-hole pores are only observed for the low power laser processed samples due to its highly focused beam and small spot size. The maximum relative density obtained for samples produced using low and high power laser was 99.3 and 99.2%, respectively, as measured using the Archimedes principle.

Crack lengths were measured for both the LP-AB and HP-AB samples that exhibited the highest relative density values. The results are summarized in Fig. 3. The average crack length does not show any trend when changing the energy density, independent on which laser was used. The main difference is the significantly longer cracks observed in samples built with the high power laser, with crack lengths averaging 150 ± 91 μm, compared to 36 ± 16 μm crack lengths in samples built with the low power laser.

Optimized energy densities, yielding samples with the highest relative densities and the lowest average crack lengths, were 45 and 60 J/mm$^3$ for the low and high power laser beams, respectively. These conditions were selected to build the tensile test specimens, hereafter labelled LP-AB and HP-AB samples. Half of the samples were subjected to a HIP post-process. After HIP, the density increased to 99.6% and all cracks were completely closed. The samples that underwent a post HIP treatment will be labelled as LP-HIP and HP-HIP samples, depending on whether they were previously SLM processed using a low or high power laser beam, respectively.

### 3.2. Influence of laser beam type on melt track width

The stability of the melt tracks was evaluated by SEM imaging of the last scanned layer for both LP-AB and HP-AB samples, shown in Fig. 4a–b, respectively. As expected, the track width is significantly larger when the high power laser is used. The LP-AB sample exhibits 100–120 μm wide tracks, while the track width of the HP-AB sample is around 500 μm. In addition, both samples show molten spherical particles attached to the tracks. While melting a track, spattering phenomena occur as seen in the work of Gunenthiram et al. [24] causing the full or partial ejection of molten metal spheres. Spherical particles can be observed on top of the scanned tracks in Fig. 4.

### 3.3. Influence of laser beam type on melt pool dimensions and solidification microstructure

Representative microstructures of XZ cross-sections in AB and HIP samples are shown in Fig. 5. Cracks, indicated by yellow arrows and in the zoomed inset in Fig. 5a, are present in the AB condition for both LP-AB (Fig. 5a) and HP-AB (Fig. 5b) samples. All cracks were found at grain boundaries, independent on the type of laser beam that was used. The cracks in HP-AB samples are all located parallel to BD, while for the LP-AB samples the cracks do not show a preferential direction, since the grains do not exhibit the typical elongated morphology along BD as observed in HP-AB samples.

The shape and size of the melt pools vary between samples processed with the two different lasers. LP-AB samples show hemispherical melt pools with a diameter of around 120 μm. On the other hand, HP-AB samples exhibit shallow and wide melt pools with semi-elliptical shape. The depth of the melt pools is around 120 μm and the width around 500 μm. In both LP-AB and HP-AB samples, the individual grains, which can be differentiated from each other by contrast changes within the melt pools, as observed in Fig. 4a–b, grow epitaxial through the layers.

At higher magnification, a typical cellular/dendritic solidification microstructure is found for both LP-AB and HP-AB samples, as also observed in other investigations on the same material (Fig. 5c–d) [17,19,20]. The major difference between samples processed using

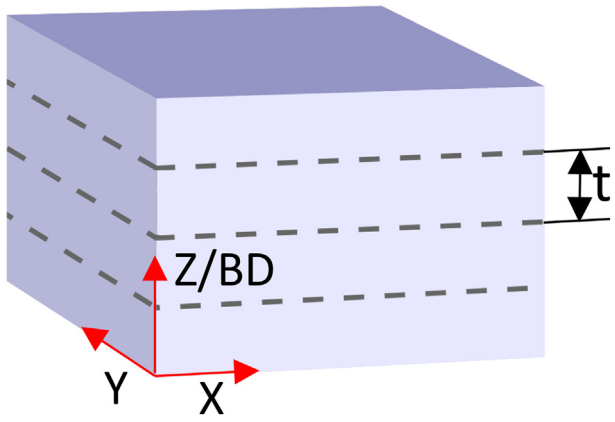


**Fig. 1.** Graphic representation of the built samples showing the coordinate axes, Z being parallel to the BD and t the layer thickness.

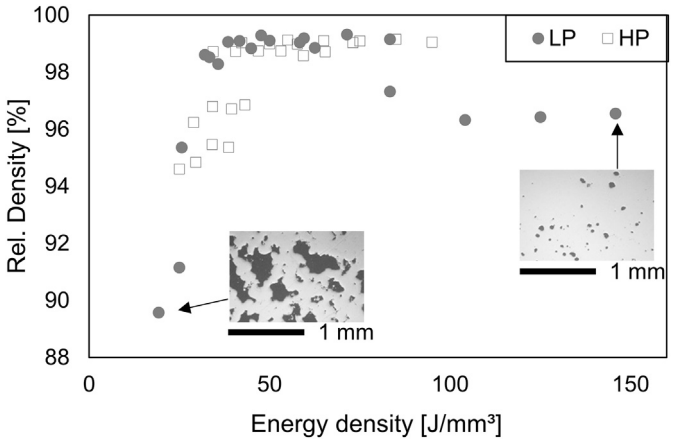


**Fig. 2.** Relative density of samples processed with low power (LP) and high power (HP) laser beams as function of the volumetric energy density. The left micrograph shows unmolten regions and the right one key-hole porosities.

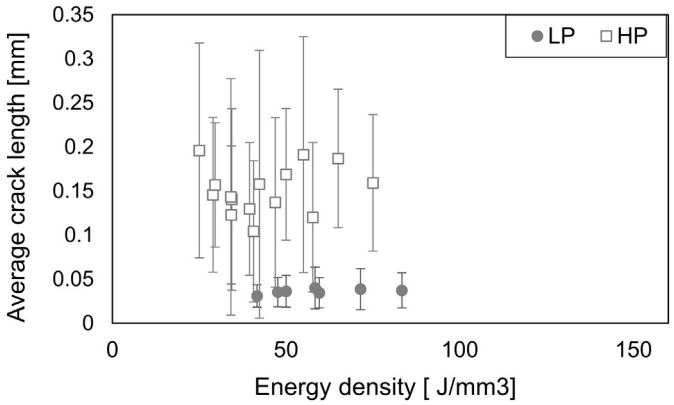


**Fig. 3.** Average crack length of samples built with LP (low power) and HP (high power) laser as function of the energy density. The cracks were measured for one cross section of 1 $mm^2$ for all samples and the average value is displayed.

different lasers is the primary dendrite spacing. LP-AB samples show a cell width of ~0.5 μm while the cell width is ~1 μm in HP-AB samples. In addition, the initiation of secondary dendrite arms in all HP-AB samples is observed. The secondary dendrite arm spacing equals ~0.5 μm in the HP-AB samples, considering the dendrites growing parallel to the polished plane (Fig. 5d) as indicated by arrows. No secondary dendrite arms are visible in LP-AB samples.

After HIP, all cracks are completely closed and the microstructure drastically changes as shown in Fig. 5e–f. The melt pool structure observed in as-built samples is not present anymore and dark coloured grain boundaries are observed by LOM after etching the samples. Moreover, the cellular/dendritic solidification microstructure has disappeared. Significantly larger grain sizes are observed in HP-HIP samples compared to LP-HIP samples.

The microstructure of both LP-AB and LP-HIP samples was also analysed using TEM. The cellular solidification structure, hereafter called cells, observed in LP-AB samples by SEM (Fig. 5c), are shown in the Bright Field (BF) TEM image on Fig. 6a but now observed perpendicular to the growth axis of the cells. The higher magnification and imaging conditions of the TEM allow to conclude that the actual cell walls are in fact dislocation cells (Fig. 6a). In the LP-HIP samples, the dislocation cells evolve into sub-grains and the dislocation density decreases significantly, contributing to a larger misorientation between coarser sub-grains (Fig. 6b). It should be mentioned that these sub-grains were not observed before using LOM or SEM (Fig. 5e,f). The same phenomena are expected to be observed for HP-AB and HP-HIP.

EBSD images are shown in Fig. 7 for all samples showing the crystallographic orientation with respect to the scanning direction. The inverse pole figures represent the texture parallel to the BD. In all samples grains growing across several layers can be observed, parallel to the Z direction. For the LP-AB sample (Fig. 7a), grains tend to grow not only parallel to the BD but some small grains also grow under 30–50° degree angles relative to the Z axis. The average grain length and width are 80 and 60 μm, respectively. On the contrary, at the XZ plane of HP-AB (Fig. 7b) all the grains grow along the Z direction and they are up to 1 mm in length and 150 μm in width.

After HIP post processing, the grain size and structure are changed compared to the AB condition. The LP-HIP sample, Fig. 7c, contains less polygonal and slightly larger grains, evolving from 80 μm in length in case of the LP-AB sample to 150 μm in case of the LP-HIP sample. In the case of the HP-HIP sample (Fig. 7d), similar coarsening occurs during HIP. The grain size is significantly larger in case of the HP-SLM samples, as compared to the low power laser processed samples.

Regarding the crystallographic orientation, the main difference is the stronger texture along the ⟨100⟩ crystal direction parallel to the BD of samples produced with the high power laser. The texture is quantified using the texture index. For isotropic materials this value equals to 1 and for anisotropic materials the value is higher than 1 [25]. HP-AB and HP-HIP samples show a texture index of 6.3 and 6.6, respectively, compared to the fairly random texture, represented by texture indices of 1.8 and 2.1 for LP-AB and LP-HIP samples, respectively. In addition, after HIP, a slight increase in texture can be observed, primarily for LP-HIP samples.

In all HIP processed samples, unresolved points were encountered at the grain boundaries, which suggests that other phases, besides the austenitic FCC phase, were formed during HIP. These phases were not detected by XRD (results not shown in this work) as they might be under the detection limit of this technique. Focussing on the grain boundaries using HAADF-STEM, some grey and light grey phases can be seen. TEM images together with the corresponding EDX mapping are shown in Fig. 8. From the corresponding numerical data it can be concluded that these phases are primarily Cr and C-rich, with minor enrichments in Mo and depletion in Ni. This was confirmed by SAED revealing a $Cr_{23}C_6$ crystal structure (zoomed inlet in Fig. 8a).

### 3.4. Mechanical properties

Micro Vickers hardness measurements were conducted for all samples and the results are displayed in Fig. 9. For both lasers, the AB samples are harder than the HIPed samples. The LP-AB sample exhibits the highest hardness with 276 ± 2 HV. In addition, for both the AB and HIP condition, low power processed samples exhibit higher hardness values than high power processed samples. Furthermore, all materials, independent on which laser beam was used, have higher hardness values compared to those reported in literature for wrought and subsequently annealed Hastelloy X (180 HV) [26].

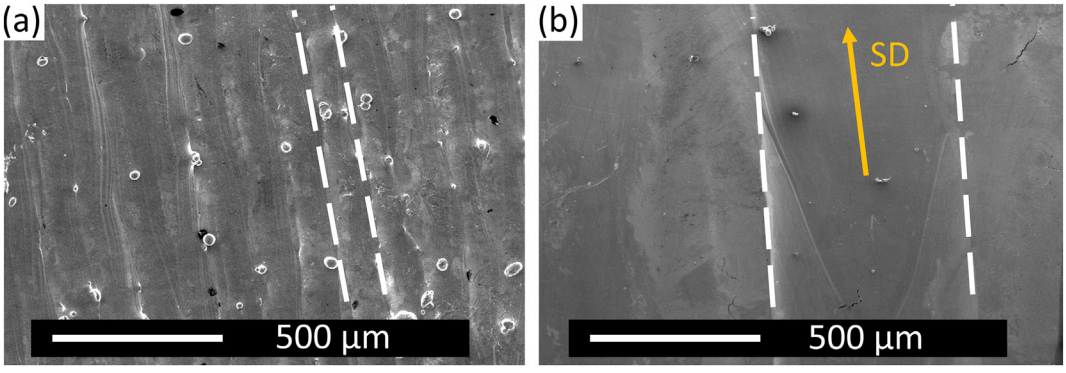


**Fig. 4.** SEM image of XY surface of LP-AB sample (a) and HP-AB sample (b) showing the molten tracks and attached particles. In the HP-AB sample the scanning direction (SD) of the track can be observed.

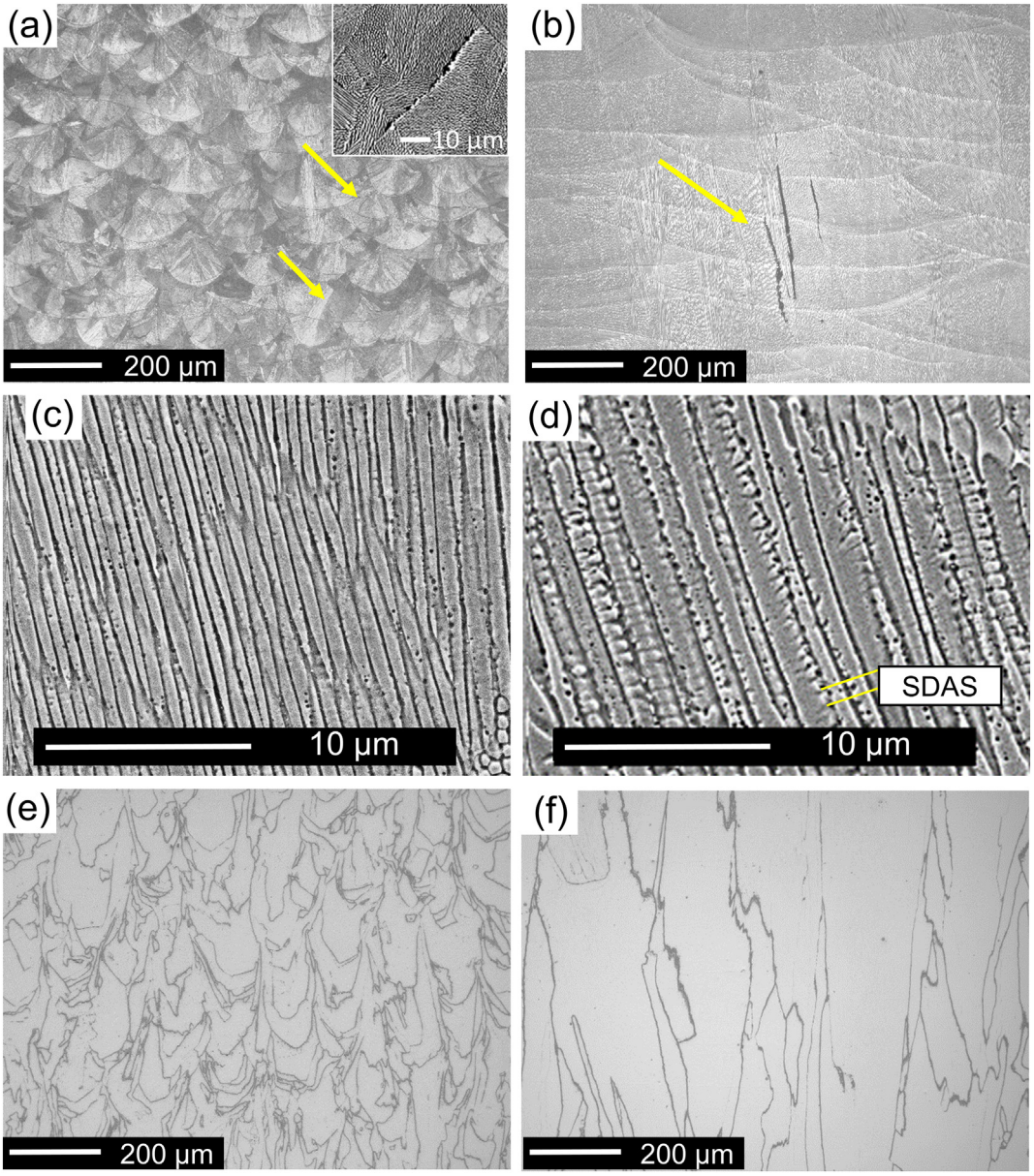


**Fig. 5.** XZ plane of LP-AB (a,c), LP-HIP (e), HP-AB (b,d) and HP-HIP (f) samples. LOM images show the melt pool structure of both lasers and the present cracks indicated by yellow arrows (a–b) and the zoomed inset in (a). SEM images show a closer look of the cells in vertical direction and secondary dendrite arm present for HP-AB (c–d). LOM images show grain boundaries after HIP (e–f).

Tensile tests were carried out for all samples built in horizontal direction, considered the most detrimental orientation due to the orientation of the cracks normal to the testing direction. Tensile properties such as yield tensile strength (YTS), ultimate tensile strength (UTS) and strain at fracture are depicted in Fig. 10 and compared to the conventionally produced Hastelloy X [26].

LP-AB samples show higher yield and ultimate tensile strength values than HP-AB samples. After HIP treatment, the yield strength decreases significantly, independent on the type of laser that was used. This tendency was also observed in the hardness values shown in Fig. 9. There also, samples subjected to HIP showed lower hardness values compared to samples tested in the as built condition. The YTS of both LP-AB, LP-HIP and HP-AB samples is significantly higher than conventionally produced Hastelloy X, while it is similar for HP-HIP samples. On the other hand, the ultimate tensile strength of conventionally produced Hastelloy X is similar to that of samples tested in the as built condition, independent on the laser type that was used. After HIP, opposite tendencies are observed: a decrease in UTS for LP-HIP and an increase for HP-HIP. This could be attributed to the high amount of cracks in HP-AB which leads to an early fracture of the material. The UTS values obtained for the LP-AB and LP-HIP samples are similar to the ones of conventional Hastelloy X.

The strain at fracture in the AB condition is lower compared to conventionally processed Hastelloy X, independent on the type of laser that was used. The lowest values are obtained for HP-AB samples with an average fracture strain of around $9 \pm 5\%$ compared to the fracture strain of LP-AB samples, exhibiting $18 \pm 4\%$. After HIP, tensile fracture strain values close to 40% are obtained for both LP-HIP and HP-HIP samples. This suggests that the cracks present in HP-AB samples have a large effect on the ductility and cause early fracture. After closing the cracks during HIP, fracture strain values close to the ones obtained for conventional Hastelloy X (45.5%) [26] are obtained for both low and high power laser processed materials. The decrease in dislocation density found after HIP also contributed to the increase of the strain of the specimens.

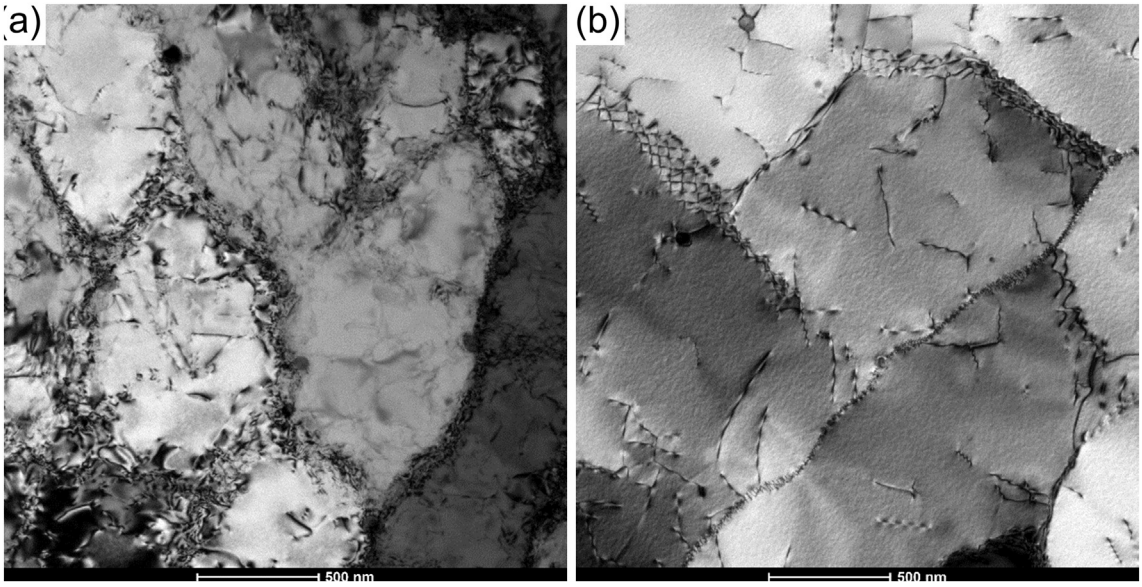


**Fig. 6.** BF-TEM images of LP-AB sample showing dislocation cells with tangled dislocations on dislocation walls (a) and LP-HIP sample in which dislocation cells have turned into sub-grains with larger misorientation, sharper interfaces and coarser size (b).

### 3.5. Fractography

The fracture surfaces of samples built with the high power laser are shown in Fig. 11. The HP-AB sample shows interconnected cracks parallel to the building direction indicated by an arrow. In addition, two zones can be distinguished as ductile-like and brittle-like zones, labelled zones 1 and 2 respectively. In the ductile zone 1, dimples of around 2 μm in diameter can be found as can be seen in Figs. 11c and 10e. Upon more detailed investigation, the brittle-like zone 2 shows the cellular dendritic solidification morphology within the fracture surface (Fig. 11d). The solidification structure is found inside the cracks, indicating that it is not a fracture feature. This suggests that several 2D cracks or crack

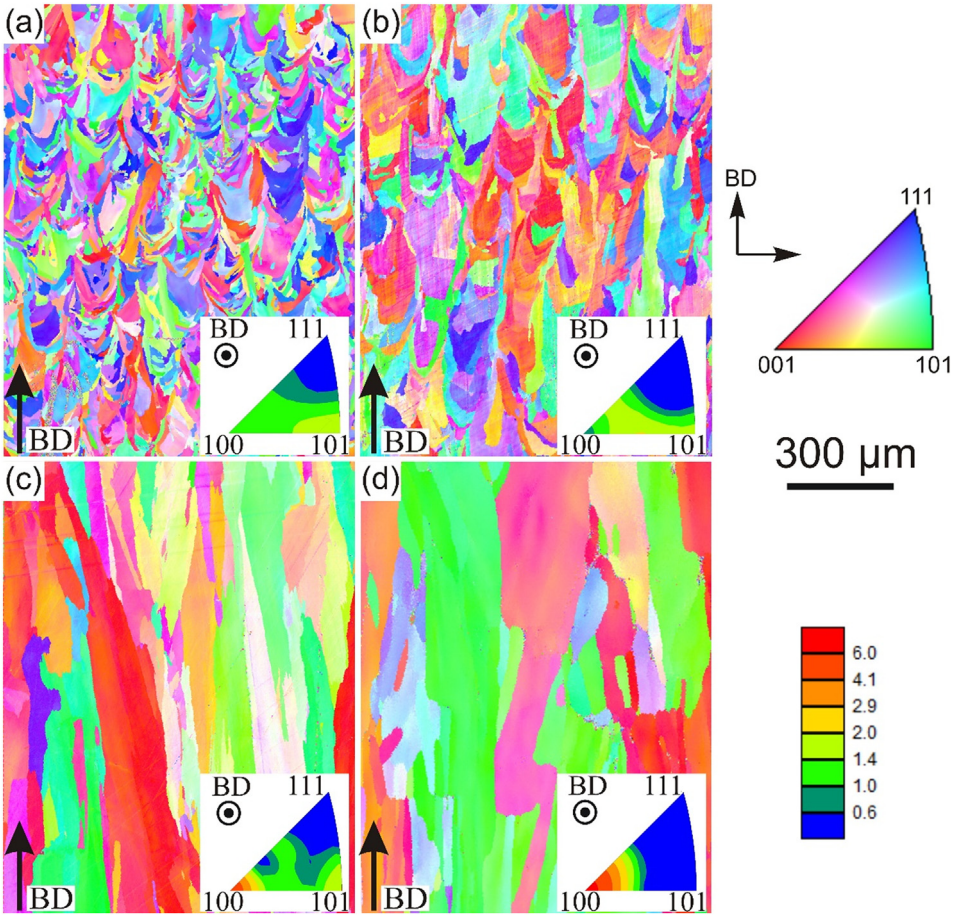


**Fig. 7.** EBSD images XZ plane (parallel to BD), of LP-AB (a), LP-HIP (b), HP-AB (c) and HP-HIP (d), with their respective inverse pole figures with respect to BD.

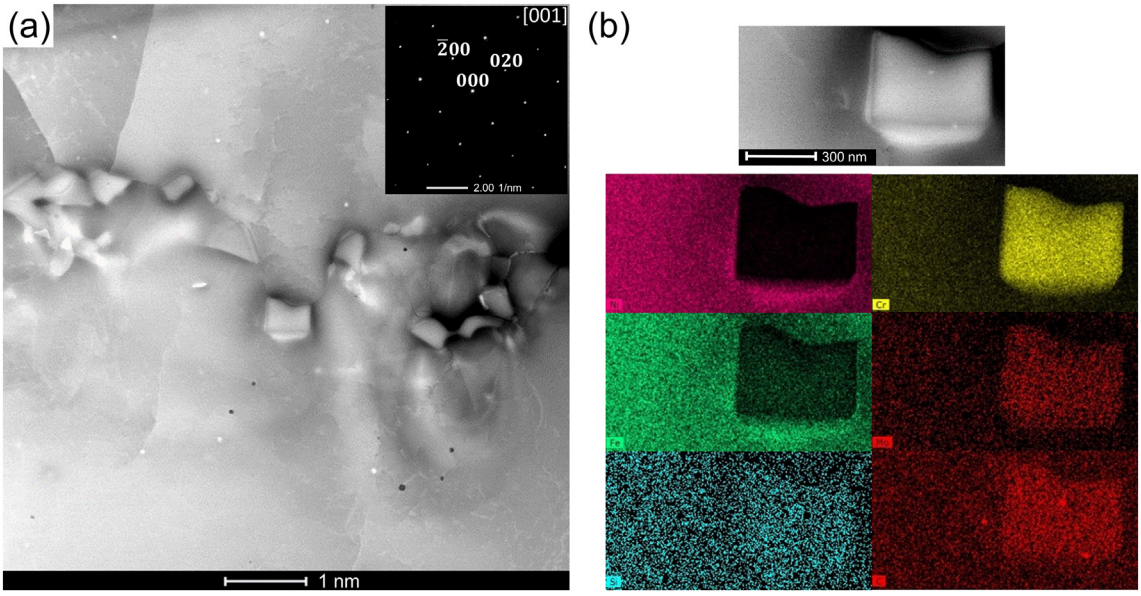


**Fig. 8.** HAADF-STEM image of $Cr_{23}C_6$ carbide at the grain boundary of LP-HIP together with the Ni, Cr, Fe, Mo, Si and C EDX mappings of the same area.

planes grew normal to the testing direction, causing the early fracture of the material. It should be noted that the cracks present in LP-AB (Fig. 5a) and HP-AB processed materials (Fig. 5b) are 2D cavities although only 1D lines can be observed in the LOM images. This also confirms that the formation of cracking occurs during solidification and not during cooling. In the LP-AB samples, similar brittle areas were found although not as often as in HP-AB samples. On the other hand, the HP-HIP samples (Fig. 11b) show only ductile failure as many 2 μm wide dimples were found on the fracture surface.

## 4. Discussion

### *4.1. Comparison between low power and high power processed samples*

The objective of using HP-SLM is the significant increase in productivity, thanks to the increased layer thickness and hatch spacing. This is the reason why machine suppliers are recently adding more lasers or higher power lasers to the industrial SLM machines. However, the real impact of the use of a high power laser on the microstructure and mechanical properties of Hastelloy X has not yet been reported. In this work, the SLM productivity has been increased from 6 $mm^3/s$, when a low power laser was used, to 16 $mm^3/s$, when a high power laser was used, i.e. a 2.6 times more efficient production process.

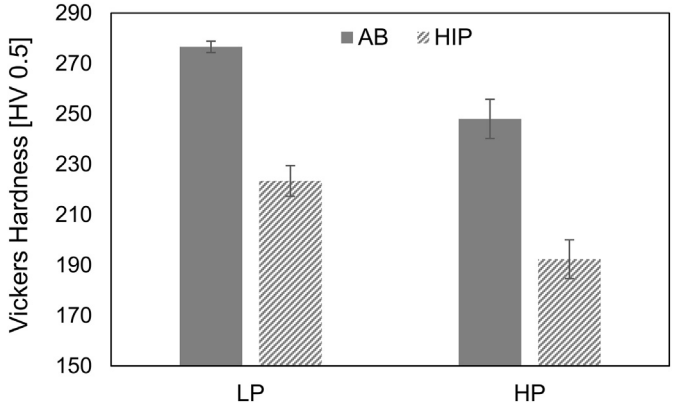


**Fig. 9.** Micro Vickers hardness of AB and HIP samples produced with low (LP) and high (HP) power laser.

This work has shown that the use of different lasers with different laser power, spot size and laser power distribution, induces completely different microstructures when the same material is processed by SLM. In addition, the crack density proves to be different, e.g., a smaller amount and size of cracks was found for samples built with the low power laser compared to materials built with a high power laser. Nevertheless, it was observed that comparable energy densities can be used for different types of lasers when aiming at densities above 99%.

At the melt pool scale, the main difference between both lasers is the melt pool shape. Different heat gradient directions result in different grain morphologies as shown in Fig. 12. During solidification, grains grow along the heat gradient and also perpendicular to the melt pool border [27]. For LP-AB samples (Fig. 12a), processed with a Gaussian and narrow laser beam, the heat gradient in a single scan track (ST) occurs in the radial direction. After a second track (ST2) is scanned, mainly the bottom of the previous melt pool remains. As seen in Fig. 12a, after scanning several tracks, a vertical and slightly angled heat flow direction is predominant. This explains the tendency for having vertically grown grains along with other grains oriented a few degrees off the z direction. In the case of HP-AB samples (Fig. 12b), processed with a top-hat and wide laser beam, the heat gradient is mostly in the vertical direction even for a single track. Therefore, the morphological texture parallel to the vertical direction is more pronounced in HP-AB samples. Moreover, the same reasoning can be applied to explain the stronger crystallographic texture observed in HP-AB samples. The horizontal melt pool border, and the predominantly vertically oriented heat flow direction is favourable for ⟨100⟩ crystal growth in the build direction (Z). These findings are in agreement with the observations reported by Niendorf et al. for 316 L [13] and Popovich et al. for IN718 [28] when using HP-SLM process.

At a more microscopic scale, microstructural differences were also observed when comparing the LP-AB and HP-AB samples, as seen in Fig. 5c,d. When building with the low power laser, only primary dendrite arms with an average diameter of 0.5 μm were observed. However, in the HP-AB samples, the primary dendrite arms exhibit dendrite arm diameters of 1–2 μm. The solidification structure observed in HP-AB samples suggests that the parameters used lead to a lower temperature gradient (G) and/or larger growth rate (R). Hence the cooling rate (GxR)

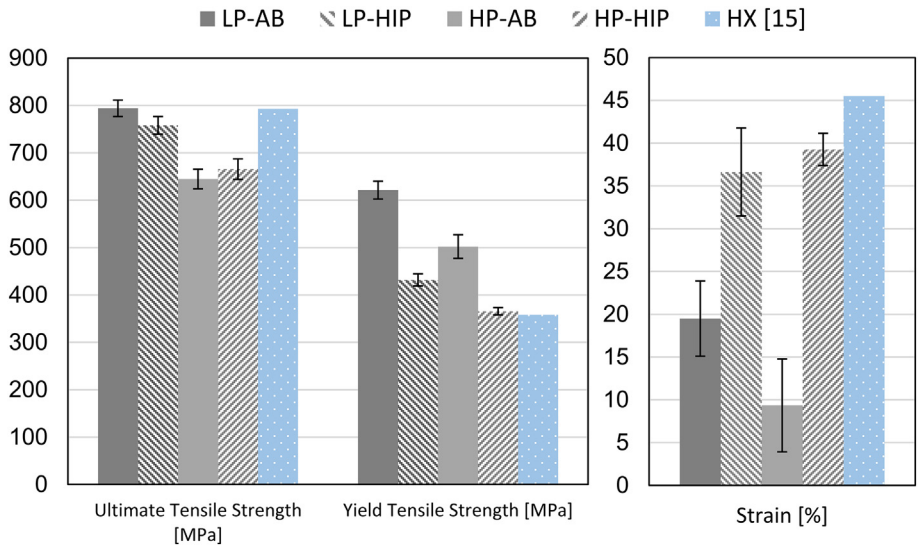


**Fig. 10.** Tensile properties of LP-AB, LP-HIP, HP-AB and HP-HIP compared to conventional Hastelloy X [15].

is lower for samples built using the high power laser than for low power laser processed samples, which results in coarser cells and growth of small secondary dendrite arms.

In addition, the lower hardness (Fig. 9) and tensile yield strength (Fig. 10) observed for the HP-AB can be attributed to the larger cell size. As it was shown in Fig. 6, the cell boundaries are decorated by a

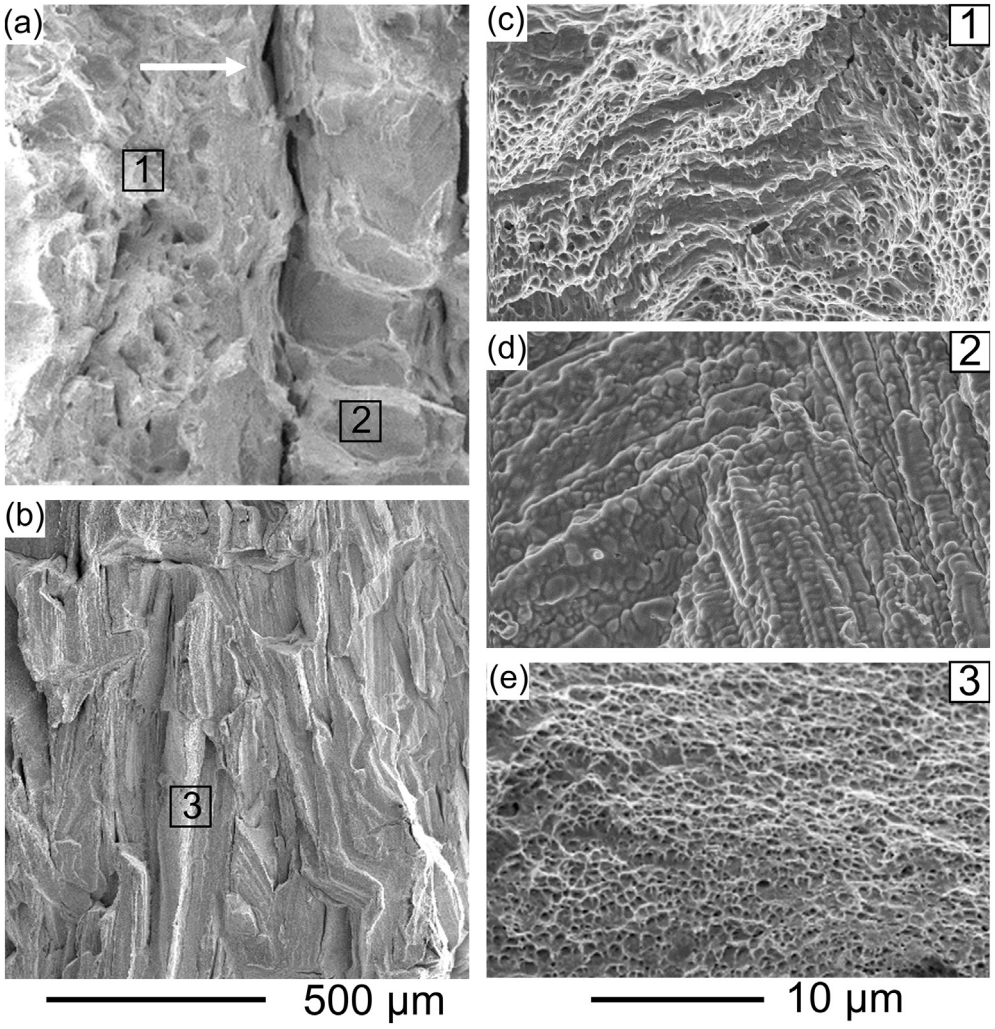


**Fig. 11.** Fracture surfaces of HP-AB (a) and HP-HIP (b) samples after tensile testing. Detailed micrographs of zones 1, 2 and 3 are shown in panels (c–e). Areas 1 (c) and 3 (e) show a ductile fracture surface, while the dendritic solidification structure, observed on the fracture surface of the HP-AB samples, is seen in area 2 (d).

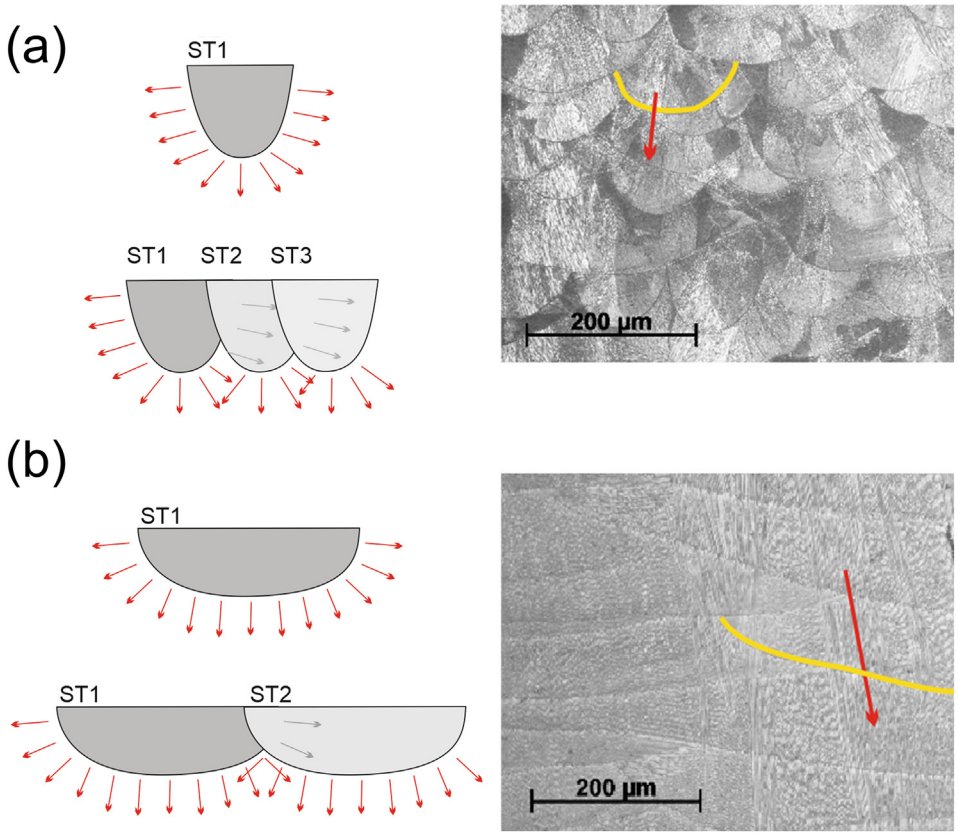


**Fig. 12.** Heat gradient representation for the two different melt pool shapes obtained for samples produced with low (a) and high power (b) samples.

high density of dislocations, creating a dislocation wall impeding dislocation movement. Therefore, the smaller cell and grain size found in LP-AB samples, resulting in high hardness and yield strength values, goes in accordance with the Hall-Petch Eq. (2)

$$\sigma_y = \sigma_0 + \frac{k_y}{\sqrt{d}} \text{ [MPa]} \quad (2)$$

where $\sigma_y$ is the yield strength of the material [MPa], $\sigma_0$ is the frictional stress for dislocation movement [MPa], $k_y$ is the Hall-Petch parameter for the material [MPa $m^{1/2}$] and $d$ is the average grain diameter [m].

The strain at fracture of HP-AB samples is lower compared to that of LP-AB samples. This cannot be attributed only to the microstructure. Therefore, it is clear that the amount of cracks present in both samples influenced the tensile strain of the as built parts. HP-AB samples contain longer and wider cracks normal to the testing direction, as compared to LP-AB samples. It should be noted that horizontally built Hastelloy X samples only show 9% fracture strain, even when crack free samples were produced [22]. As seen in the fracture surfaces (Fig. 11a) of HP-AB samples, a large fraction of the fracture surface areas shows a dendritic microstructure. This confirms that the fracture was caused by the solidification cracks that were torn apart. This also explains the lower strain and early fracture observed for HP-AB samples. On the other hand, it should be noted that, besides the presence of micro cracks within LP-AB samples, the obtained mechanical properties are comparable to the ones produced by conventional means.

### *4.2. Effect of the hot isostatic pressing post-processing*

Hot isostatic pressing (HIP) has been proven to be a necessary and beneficial post process treatment. The porosity content was reduced for both LP-HIP and HP-HIP samples. Cracks were also completely closed in both cases, hence increasing the strain at fracture of the parts.

The microstructure after HIP has changed significantly. At a macroscopic level, the melt pool boundaries, observed within the as built condition, are not present anymore after HIP independent on the type of laser that was used. Slightly coarser grains were observed after HIP. It is thought that grains with similar crystal orientation merge during HIP, hence coarsening the microstructure, as observed for LP-HIP and HP-HIP samples.

At microscopic scale, dislocation cells that were observed in the AB condition, were not present after the applied HIP treatment as shown in Fig. 5e–f using LOM or SEM. However, they could be observed by TEM. The partial recovery annealing of the dislocations and the slightly increased cell size after HIP play a major role in the lower YTS and hardness values obtained with respect to the AB condition.

During the HIP treatment, the formation of chromium and molybdenum enriched carbides, was observed. The precipitation of such carbides decreases the Cr and Mo content within the matrix [29,30]. This phenomenon decreases the extent of solid solution strengthening within the matrix, and hence explains the Vickers hardness and yield strength decrease of both the LP-HIP and HP-HIP samples. In addition to this, the decrease in dislocation density will contribute to the hardness decrease after HIP. Nevertheless, the hardness values of the LP-HIP and HP-HIP samples still outperformed the wrought annealed Hastelloy X (180 HV) reference samples [26], probably thanks to the remaining sub-grain boundaries.

## 5. Conclusions

The present work has studied the influence of low power and high power lasers on the microstructure and mechanical properties of SLM processed Hastelloy X.

When a high power laser with broad beam diameter is used, the cooling rate during SLM is decreased, hence increasing the cell and grain size. The coarsened microstructure reduced the hardness and

yield strength of high power processed samples compared to low power processed samples. The top-hat power distribution of the high power laser, in combination with a 10 times larger laser spot size as compared to the 70 μm diameter low power laser with Gaussian power profile, results in the formation of wide and shallow melt pools. In contrast, samples built with the low power laser, present narrow and deep melt pools. The melt pool shape created by the use of the high power laser enhances the formation of both a morphological and crystallographic texture along the building direction. On the contrary, low power processed samples exhibit less crystallographic and morphological texture with grains oriented not only in the build direction but also under 30–50° angles with respect to build direction.

Hot Isostatic Pressing (HIP) allowed to close all cracks that were present in as-built parts and improved the mechanical performance. After HIP, a slight increase in grain and cell size was observed along with a reduction of the dislocation density. Precipitation of Cr-rich carbides at grain boundaries was observed after HIP. Besides the increased tensile strain, the hardness and yield strength decreased after HIP. Overall, the SLM processed and post HIPed parts exhibit quasi-static mechanical properties that are comparable to wrought annealed Hastelloy X.

## CRediT authorship contribution statement

**Maria L. Montero-Sistiaga:** Conceptualization, Data curation, Investigation, Methodology, Visualization, Writing - original draft, Writing - review & editing. **Saeid Pourbabak:** Visualization, Methodology, Investigation, Writing - review & editing. **Jan Van Humbeeck:** Funding acquisition, Supervision, Validation, Writing - review & editing. **Dominique Schryvers:** Funding acquisition, Supervision, Validation, Writing - review & editing. **Kim Vanmeensel:** Funding acquisition, Supervision, Project administration, Validation, Writing - review & editing.

## CRediT authorship contribution statement

**Maria L. Montero-Sistiaga:** Conceptualization, Data curation, Investigation, Methodology, Visualization, Writing - original draft, Writing - review & editing. **Saeid Pourbabak:** Visualization, Methodology, Investigation, Writing - review & editing. **Jan Van Humbeeck:** Funding acquisition, Supervision, Validation, Writing - review & editing. **Dominique Schryvers:** Funding acquisition, Supervision, Validation, Writing - review & editing. **Kim Vanmeensel:** Funding acquisition, Supervision, Project administration, Validation, Writing - review & editing.

## Acknowledgements

This research was supported by the ENGIE Research and Technology Division. The authors acknowledge ENGIE Research and Technology Division for the use of the SLM280HL machine. S.P. likes to thank the Flemish Science Foundation FWO for financial support under Project G.0366.15N.

## References

[1] J.-P. Kruth, G. Levy, F. Klocke, T.H.C. Childs, Consolidation phenomena in laser and powder-bed based layered manufacturing, CIRP Ann. Manuf. Technol. 56 (2007) 730–759, https://doi.org/10.1016/j.cirp.2007.10.004.
[2] I. Yadroitsev, A. Gusarov, I. Yadroitsava, I. Smurov, Single track formation in selective laser melting of metal powders, J. Mater. Process. Technol. 210 (2010) 1624–1631, https://doi.org/10.1016/j.jmatprotec.2010.05.010.
[3] L. Thijs, F. Verhaeghe, T. Craeghs, J. Van Humbeeck, J.-P. Kruth, A study of the microstructural evolution during selective laser melting of Ti–6Al–4V, Acta Mater. 58 (2010) 3303–3312, https://doi.org/10.1016/j.actamat.2010.02.004.
[4] E. Yasa, J.-P. Kruth, Microstructural investigation of Selective Laser Melting 316L stainless steel parts exposed to laser re-melting, Procedia Eng. 19 (2011) 389–395, https://doi.org/10.1016/j.proeng.2011.11.130.
[5] K. Kempen, Expanding the Materials Palette for Selective Laser Melting of Metals, KU Leuven, 2015.
[6] X.P. Li, X.J. Wang, M. Saunders, A. Suvorova, L.C. Zhang, Y.J. Liu, M.H. Fang, Z.H. Huang, T.B. Sercombe, A selective laser melting and solution heat treatment refined Al–12Si alloy with a controllable ultrafine eutectic microstructure and 25% tensile ductility, Acta Mater. 95 (2015) 74–82, https://doi.org/10.1016/j.actamat.2015.05.017.
[7] M. Cloots, P.J. Uggowitzer, K. Wegener, Investigations on the microstructure and crack formation of IN738LC samples processed by selective laser melting using Gaussian and doughnut profiles, Mater. Des. 89 (2016) 770–784, https://doi.org/10.1016/j.matdes.2015.10.027.
[8] T. Etter, K. Kunze, F. Geiger, H. Meidani, Reduction in mechanical anisotropy through high temperature heat treatment of Hastelloy X processed by Selective Laser Melting (SLM), IOP Conf. Ser. Mater. Sci. Eng. 82 (2015) 0–4, https://doi.org/10.1088/1757-899X/82/1/012097.
[9] G. Marchese, G. Basile, E. Bassini, A. Aversa, D. Ugues, P. Fino, S. Biamino, Study of the microstructure and cracking mechanisms of Hastelloy X produced by laser powder bed fusion, Materials (Basel) 11 (2018) 106, https://doi.org/10.3390/ma11010106.
[10] L.N. Carter, C. Martin, P.J. Withers, M.M. Attallah, The influence of the laser scan strategy on grain structure and cracking behaviour in SLM powder-bed fabricated nickel superalloy, J. Alloys Compd. 615 (2014) 338–347, https://doi.org/10.1016/j.jallcom.2014.06.172.
[11] X. Wang, L.N. Carter, B. Pang, M.M. Attallah, M.H. Loretto, Microstructure and yield strength of SLM-fabricated CM247LC Ni-superalloy, Acta Mater. 128 (2017) 87–95, https://doi.org/10.1016/J.ACTAMAT.2017.02.007.
[12] D. Buchbinder, H. Schleifenbaum, S. Heidrich, W. Meiners, J. Bültmann, High power selective laser melting (HP SLM) of aluminum parts, Phys. Procedia 12 (2011) 271–278, https://doi.org/10.1016/j.phpro.2011.03.035.
[13] T. Niendorf, S. Leuders, A. Riemer, H.A. Richard, T. Tröster, D. Schwarze, Highly anisotropic steel processed by selective laser melting, Metall. Mater. Trans. B Process Metall. Mater. Process. Sci. 44 (2013) 794–796, https://doi.org/10.1007/s11663-013-9875-z.
[14] R. Mertens, B. Vrancken, N. Holmstock, Y. Kinds, J.-P. Kruth, J. Van Humbeeck, Influence of powder bed preheating on microstructure and mechanical properties of H13 tool steel SLM parts, Phys. Procedia 83 (2016) 882–890, https://doi.org/10.1016/j.phpro.2016.08.092.
[15] W. Li, J. Liu, Y. Zhou, S. Wen, Q. Wei, C. Yan, Y. Shi, Effect of substrate preheating on the texture, phase and nanohardness of a Ti–45Al–2Cr–5Nb alloy processed by selective laser melting, Scr. Mater. 118 (2016) 13–18, https://doi.org/10.1016/j.scriptamat.2016.02.022.
[16] B. Vrancken, S. Buls, J. Kruth, J. Van Humbeeck, R. Stress, Preheating of selective laser melted Ti6Al4V: microstructure and mechanical properties, Proc. 13th World Conf. Titan. 2016, pp. 2–6, https://doi.org/10.1002/9781119296126.ch215.
[17] D. Tomus, T. Jarvis, X. Wu, J. Mei, P. Rometsch, E. Herny, J.F. Rideau, S. Vaillant, Controlling the microstructure of Hastelloy-X components manufactured by Selective Laser Melting, Phys. Procedia 41 (2013) 823–827, https://doi.org/10.1016/j.phpro.2013.03.154.
[18] F. Wang, Mechanical property study on rapid additive layer manufacture Hastelloy® X alloy by selective laser melting technology, Int. J. Adv. Manuf. Technol. 58 (2012) 545–551, https://doi.org/10.1007/s00170-011-3423-2.
[19] N.J. Harrison, I. Todd, K. Mumtaz, Reduction of micro-cracking in nickel superalloys processed by Selective Laser Melting: a fundamental alloy design approach, Acta Mater. 94 (2015) 59–68, https://doi.org/10.1016/j.actamat.2015.04.035.
[20] F. Najafzadegan, H. Mansori, M. Shamanian, Investigation of microstructure of the weld zone of Hastelloy X via pulsed Nd-YAG laser welds, J. Adv. Mater. Process. 1 (2013) 49–56.
[21] M. Pakniat, F.M. Ghaini, M.J. Torkamany, Hot cracking in laser welding of Hastelloy X with pulsed Nd:YAG and continuous wave fiber lasers, Mater. Des. 106 (2016) 177–183, https://doi.org/10.1016/j.matdes.2016.05.124.
[22] D. Tomus, Y. Tian, P.A. Rometsch, M. Heilmaier, X. Wu, Influence of post heat treatments on anisotropy of mechanical behaviour and microstructure of Hastelloy-X parts produced by selective laser melting, Mater. Sci. Eng. A 667 (2016) 42–53, https://doi.org/10.1016/J.MSEA.2016.04.086.
[23] C.T. Rueden, J. Schindelin, M.C. Hiner, B.E. DeZonia, A.E. Walter, E.T. Arena, K.W. Eliceiri, ImageJ2: ImageJ for the next generation of scientific image data, BMC Bioinformatics 18 (2017), 529. https://doi.org/10.1186/s12859-017-1934-z.
[24] V. Gunenthiram, P. Peyre, M. Schneider, M. Dal, F. Coste, R. Fabbro, Experimental analysis of spatter generation and melt-pool behavior during the powder bed laser beam melting process, J. Mater. Process. Technol. (2017)https://doi.org/10.1016/j.jmatprotec.2017.08.012.
[25] U.F. Kocks, C.N. Tome, H.-R. Wenk, Texture and Anisotropy: Preferred Orientations in Polycrystals and Their Effect on Materials Properties, Cambridge University Press, 2000.
[26] Haynes-International, Hastelloy X Alloy, High-temperature Alloy. 06002, 1997 16.
[27] S. Kou, Solidification and liquation cracking issues in welding, JOM 55 (2003) 37–42.
[28] V.A. Popovich, E.V. Borisov, A.A. Popovich, V.S. Sufiiarov, D.V. Masaylo, L. Alzine, Functionally graded Inconel 718 processed by additive manufacturing: crystallographic texture, anisotropy of microstructure and mechanical properties, Mater. Des. 114 (2016) 441–449, https://doi.org/10.1016/j.matdes.2016.10.075.
[29] R. Hu, G. Bai, J. Li, J. Zhang, T. Zhang, H. Fu, Precipitation behavior of grain boundary M23C6 and its effect on tensile properties of Ni–Cr–W based superalloy, Mater. Sci. Eng. A 548 (2012) 83–88, https://doi.org/10.1016/J.MSEA.2012.03.092.
[30] W. Li, X. Chen, L. Yan, J. Zhang, X. Zhang, F. Liou, Additive manufacturing of a new Fe-Cr-Ni alloy with gradually changing compositions with elemental powder mixes and thermodynamic calculation, Int. J. Adv. Manuf. Technol. (2017)https://doi.org/10.1007/s00170-017-1302-1.